



**Unveiling the Mechanism of the Photocatalytic Reduction of
CO₂ to Formate Promoted by Porphyrinic Zr-Based Metal-
Organic Frameworks**

Journal:	<i>Journal of Materials Chemistry A</i>
Manuscript ID	TA-ART-05-2022-004164.R1
Article Type:	Paper
Date Submitted by the Author:	27-Jul-2022
Complete List of Authors:	<p>Benseghir, Youven; Collège de France, Laboratoire de Chimie des Processus Biologiques Solé-Daura, Albert; Collège de France, Laboratoire de Chimie des Processus Biologiques Cairnie, Daniel; Virginia Tech, Chemistry Robinson, Amanda; Collège de France, Laboratoire de Chimie des Processus Biologiques Duguet, Mathis; Collège de France, Laboratoire de Chimie des Processus Biologiques; Institut Lavoisier de Versailles, Chimie Processus Biologiques Mialane, Pierre; Institut Lavoisier de Versailles, Chemistry Gairola, Priyanka; Institut Lavoisier de Versailles Gomez-Mingot, Maria; Collège de France, Laboratoire de Chimie des Processus Biologiques Fontecave, Marc; Collège de France, Chimie des Processus Biologiques Iovan, Diana; Virginia Tech, Chemistry Bonnett, Brittany; Virginia Tech, Chemistry Morris, Amanda; Virginia Tech, Chemistry Dolbecq, Anne; Institut Lavoisier de Versailles Mellot-Draznieks, Caroline; Collège de France, Chimie Processus Biologiques</p>

ARTICLE

Unveiling the Mechanism of the Photocatalytic Reduction of CO₂ to Formate Promoted by Porphyrinic Zr-Based Metal-Organic Frameworks

Received 00th January 20xx,
Accepted 00th January 20xx

DOI: 10.1039/x0xx00000x

Youven Benseghir,^{a,b,‡} Albert Solé-Daura,^{a,‡} Daniel R. Cairnie,^{c,‡} Amanda L. Robinson,^a Mathis Duguet,^{a,b} Pierre Mialane,^{*,b} Priyanka Gairola,^{b,d} Maria Gomez-Mingot,^a Marc Fontecave,^a Diana Iovan,^c Brittany Bonnett,^c Amanda J. Morris,^{*,c} Anne Dolbecq^b and Caroline Mellot-Draznieks^{*,a}

A complete picture of the reaction mechanism responsible for the photocatalytic reduction of CO₂ into formate promoted by Zr-based porphyrinic MOF-545 (PCN-222) in acetonitrile/triethanolamine (CH₃CN/TEOA) solutions is provided for the first time by combining experimental and computational approaches. Firstly, we combined the metalation of the porphyrin linkers and the synthesis under microwave conditions of nano-sized materials (150–200 nm) to reach one of the highest CO₂RR activities under visible light irradiation reported so far for a MOF-based catalyst in terms of formate production (identified in all cases as the sole product), i.e., 6000 μmol g⁻¹ after 4 h for the NanoMOF-545(Fe). A thorough mechanistic study of CO₂RR is provided afterwards, which elucidated the respective roles of TEOA, the porphyrin linkers and Zr₆-nodes. Photophysical measurements of both metalated and unmetalated MOFs excluded the prevailing belief of ligand-to-Zr₆ cluster charge-transfer states formation, while bulk photolysis proved that the porphyrinic linkers of the MOF promotes the photooxidation of TEOA under catalytic conditions. DFT calculations allowed characterizing with atomistic detail a novel reaction mechanism whereby TEOA* radicals generated photochemically at the porphyrinic linkers play the crucial role of transferring a formal hydride to a CO₂ molecule activated on a Zr^{IV} center, which acts as a Lewis acid. Notably, this mechanism backed by additional experimental assays explains the experimental activity trends observed upon metalation, on the basis of the ability of the materials to accomplish the photo-oxidation of TEOA. While elucidating the reaction pathways at work in Zr₆-based MOFs with chromophore linkers, the findings reported herein pinpoint new mechanistic features capable of rationalizing other light-driven reactions making use of TEOA (or structurally related donors) and ultimately, inspire the bottom-up design of new catalysts and catalytic routes.

Introduction

The one-way causality between greenhouse gases and the annual global mean surface temperature anomalies is now well-established, and among them, CO₂ is the main driver.¹ Reducing CO₂ emissions will thus be one of the critical challenges in the decades to come. Several technologies have been identified as capable of delivering carbon dioxide removal at scale.² Nevertheless, while CO₂ conversion is not a silver bullet to solve the CO₂ mitigation problem, this strategy should play a key role in the transition to a sustainable future in particular as it can enable the transformation of CO₂ - used as a costless C1-

feedstock - into high added-value synthetic fuels.³ To date, thermocatalysis,^{4,5} electrocatalysis,^{6–8} photocatalysis,^{9,10} radiolysis¹¹ as well as photoelectro-chemical^{12–14} and biochemical^{15,16} techniques have been used for CO₂ conversion. Targeting photocatalysis, semiconductors, molecular complexes and metal-organic frameworks (MOFs) – or their combination – have been particularly considered for the photochemical CO₂ reduction reaction (CO₂RR).^{17–19} Importantly, MOFs based on metal clusters (nodes) and multidentate organic ligands (linkers), which act as antenna upon illumination, do not require additional noble metal-based photosensitizers (PSs), bypassing the largely used [Ru(bpy)₃]²⁺ for photocatalytic applications. In a seminal example, Fu *et al.* reported that the photosensitive aminated 2-aminoterephthalate linker of the NH₂-MIL-125(Ti) MOF enables the photoreduction of CO₂ to formate under visible light irradiation in the absence of any additional PS, using triethanolamine (TEOA) as a sacrificial donor.²⁰ In similar conditions, NH₂-UiO-66(Zr) was shown to exhibit CO₂ to formate conversion upon visible-light irradiation.²¹ Zirconium MOFs made of porphyrin linkers²² as photoactive components emerged soon after these reports as a particularly attractive sub-family of MOFs for CO₂RR. First exemplified with MOF-525

^a Laboratoire de Chimie des Processus Biologiques, UMR CNRS 8229, Collège de France, Sorbonne Université, PSL Research University, 11 Place Marcelin Berthelot, 75231 Paris Cedex 05, France. E-mail: caroline.mellot-draznieks@college-de-france.fr

^b Université Paris-Saclay, UVSQ, CNRS UMR 8180, Institut Lavoisier de Versailles, 78000 Versailles, France. E-mail: pierre.mialane@uvsq.fr

^c Department of Chemistry, Virginia Tech, Blacksburg, Virginia, 24060, USA. E-mail: ajmorris@vt.edu

^d Institut de Chimie Moléculaire et des Matériaux d'Orsay, CNRS, Université Paris-Sud, Université Paris-Saclay, F-91405 Orsay, France.

‡ These authors contributed equally.

Electronic Supplementary Information (ESI) available: experimental and computational details. See DOI: 10.1039/x0xx00000x

and then MOF-545, which are both built of tetrakis(4-carboxyphenyl)porphyrin (TCPP) linkers connecting Zr₆ nodes, such MOFs photoreduce CO₂ into either CO and methane^{23,24} or into formate,²⁵ respectively. Further improved catalytic performances were reported either through post-synthetic metalation of the TCPP linkers,^{23,26,27} or via partial substitution of Zr^{IV} by Ti^{IV} cations.²⁸

Thus far, several hypotheses have been evoked regarding the mechanisms involved in the photocatalytic CO₂RR by porphyrinic MOFs. Inspired by the photoinduced linker-to-node charge transfer occurring in the aminated Ti-MIL-125,²⁹ it has been proposed that the photoexcited porphyrin linker of MOF-545(Zn) may transfer an electron to the Zr^{IV}₆ node. This leads to the assumption that reduced Zr^{III} species²⁵ could form in a similar fashion as proposed for the NH₂-UiO-66(Zr) catalyst,²¹ being thus the catalytically active reducing centres. However, the occurrence of linker-to-metal charge transfer in Zr-based porphyrinic MOFs has been a matter of debate in the literature.^{30–35} Conversely, some authors assigned the CO₂RR photocatalytic activity of porphyrinic MOF to the metalated porphyrins rather than to the Zr nodes,²³ while others proposed dual routes whereby both the metalated porphyrin and the Zr₆ clusters act as active catalytic sites.³⁶ Overall, although many efforts have been devoted to investigating the catalytic properties of this family of materials, the mechanisms underlying their activities for CO₂RR are still the subject of intense debate. As such, the respective possible roles of the porphyrin linkers and of the Zr metal centres of the inorganic nodes remain to be elucidated.

Herein, we initially explored the metalation (Mn^{III}, Fe^{III}, Co^{II}, Cu^{II}, Zn^{II}) of the Zr-based porphyrinic MOF-545 to combine it, for the first time, with the nanosized scale synthesis³⁷ of MOF-545(TM) (TM = transition metal). The complementary strategies boost the targeted photocatalytic activity towards the visible-light driven reduction of CO₂ to formate in acetonitrile:TEOA mixtures. We then provide the first complete picture of the reaction mechanism with atomic detail. We carried out a comprehensive mechanistic investigation by combining spectroscopic and photophysical techniques with theoretical Density Functional Theory (DFT) calculations and additional photocatalytic assays, allowing us to characterize an unprecedented reaction mechanism for CO₂ reduction into formate. In addition to elucidating the respective roles of the porphyrin linker and the Zr₆-nodes, our findings reveal a new unexpected role for TEOA, acting as a hydride-donor species upon photo-oxidation. Aside from shedding new light on the photocatalytic activity of the porphyrinic MOF-545, this knowledge might open avenues toward understanding the large range of photocatalytic processes using TEOA as a sacrificial donor.

Results and discussion

1. Preparation and characterization of metalated and nanosized MOF-545 catalysts.

MOF-545, shown in Figure 1a with its organic and inorganic components, was synthesized following a reported synthetic

procedure using 1,2-dichloroacetic acid as a modulator.³⁸ Metalated MOF-545(TM) (TM= Mn^{III}, Fe^{III}, Co^{II}, Cu^{II}, Zn^{II}) were obtained via an analogous protocol while using the required (TM)TCPP ligand instead of the unmetalated porphyrin derivative as the starting reactant. Powder X-ray diffraction (PXRD) patterns (Figure S1) and infrared (IR) spectra (Figure S2) support the formation of the targeted materials with the MOF's characteristic peaks (see SI for details). Solid-state UV-Vis spectra evidence the porphyrin ligands Soret band at ca. 420 nm and the four Q bands in the 500–800 nm range (Figure S3).

In addition to the syntheses described above, the synthesis of nanocrystalline MOF-545(Fe) was achieved via a new microwave protocol. The synthesis of nanosized crystals of unmetalated MOF-545 was reported in DMF at 130 °C by high-throughput screening³⁹ and later applied for the preparation of nanocomposite reverse osmosis membranes.⁴⁰ Moreover, the use of various amounts of acetic acid as a modulator in DMF at 65 °C was reported to allow for the control of the crystals' size.⁴¹

However, the reported yields were rather low in both syntheses. To our knowledge, there has been no report on the

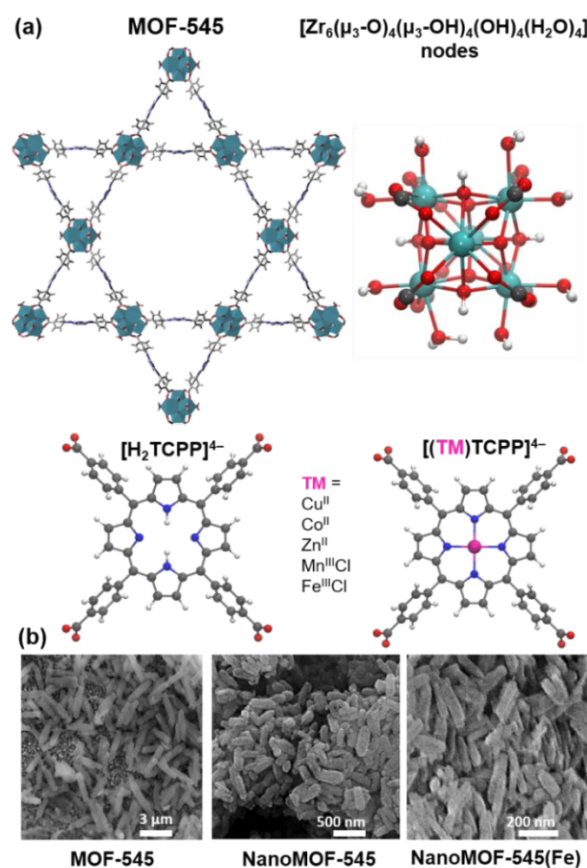


Figure 1. a) Crystal structure of MOF-545 and closer look to its organic (linkers) and inorganic (nodes) components. Colour code: Zr (cyan), O (red), C (gray), N (blue), H (white) incorporated TM ion into the porphyrinic linker (magenta). In the case of the Mn- and Fe-containing MOFs, the cationic metal centre is coordinated to a Cl anion; b) SEM images of MOF-545 (left), NanoMOF-545 (middle) and NanoMOF-545(Fe) (right).

synthesis of nanosized MOF-545(Fe) so far. We thus developed a synthetic protocol to obtain NanoMOF-545 and NanoMOF-545(Fe) under microwave conditions (130 °C, 800 W, 20 min) in good yield (see Experimental section). Their PXRD patterns

were found in full agreement with those of MOF-545 with an expected widening of the Bragg peaks (Figure S1c). SEM images indicate sizes of ca. 3000, 200 and 150 nm for MOF-545, NanoMOF-545 and NanoMOF-545(Fe), respectively (Figure 1b). A full-characterisation of the catalytic materials is described in the supplementary information, including EDX, FT-IR, UV-Vis spectra, TGA, N₂ adsorption/desorption isotherms and XPS analyses (Figures S2-S6).

2. Photocatalytic reduction of CO₂.

The photocatalytic activities for CO₂RR of the MOF-545(TM) series of solids were investigated in acetonitrile with TEOA as sacrificial electron/proton donor under visible light illumination with a 280 W Xe arc lamp. Only formate was formed and no other product, such as H₂, CO or CH₄ could be observed. A series of control experiments were performed with one component missing in each test, i.e., light, TEOA, the photocatalyst (here the MOF) or CO₂, showing there was no significant formate production (Table S1). Amongst the MOF-545(M) series, the production of HCOO⁻ increased with TM = Cu < Co < Mn < Zn < Fe, reaching a maximum of 2264 μmol g⁻¹ after 4 h with the MOF-545(Fe) photocatalyst (Figure 2). The MOF-545(Fe) was thus selected for investigating further the effect of nanosized particles on the photocatalytic performances of metalated MOF for CO₂RR. NanoMOF-545(Fe) exhibited a remarkable formate production of 4640 μmol g⁻¹ after 4 h, well above that of MOF-545(Fe) (Figure 2). This value exceeds by far those reported to date for almost all MOF-based photocatalytic systems operating under visible light (Table S2). Similarly, the unmetalated NanoMOF-545 exhibited a higher activity than MOF-545 (1600 vs 636 μmol g⁻¹ after 4 h) (Figure 2). This can be ascribed to the higher density of catalytic sites accessible to CO₂ and shorter diffusion distances. Overall, the above results highlight how the photocatalytic activity of MOF-545(TM) for CO₂RR can be tuned by playing both on the nature of the porphyrin metal centre and the size of particles.

Of note, we realized that a significant amount of the formate produced during the catalytic process remained adsorbed to the MOF, as the result of the strong affinity of the formate product for the Zr centres of the MOF.^{38,41} More precise formate yields for NanoMOF-545(Fe) were thus obtained by adding the amount of formate produced as measured in the supernatant to that retrieved upon washing the MOF with water at 60 °C, this at the end of each photocatalytic test. By doing so, the visible light-driven formate production with NanoMOF(Fe) accounted for a remarkable value of 6000 μmol g⁻¹ after 4 h (see pale-green bar in Figure 2 and Figure S7a). Finally, recyclability experiments were conducted over three runs (Figure S7b), showing only a slight decrease in activity (91% and 88% of formate production, respectively). Post-catalytic PXRD of NanoMOF-545(Fe) did not show any significant loss of crystallinity (Figure S8). We thus believe that such decrease mainly emanates from the slight mass losses along the recovery of the catalyst of the runs.

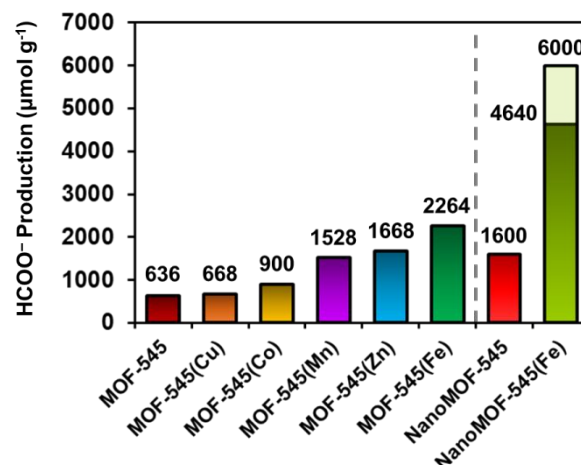


Figure 2. Formate production after 4 h for MOF-545 (dark red), MOF-545(Cu) (orange), MOF-545(Co) (yellow), MOF-545(Mn) (violet), MOF-545(Zn) (blue), MOF-545(Fe) (dark green), NanoMOF-545 (light red), and NanoMOF-545(Fe) (light green), normalized per g of catalyst. The superimposed bar in pale green for NanoMOF-545(Fe) shows the formate production measured after washing steps (see text for details). Reaction conditions: catalyst 2 mg, CH₃CN/TEOA (10:1) 2 mL ($\lambda > 415$ nm, 280 W).

3. Mechanistic study.

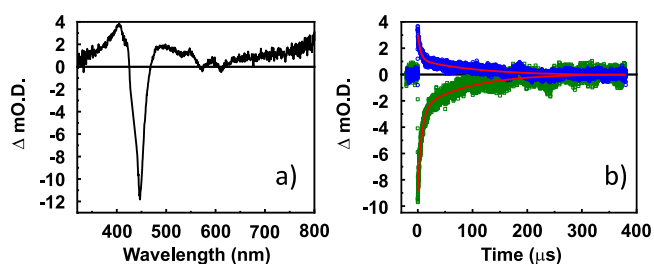
Aiming to understand the reaction mechanism governing the photoreduction of CO₂ into formate catalysed by MOF-545 and its metalated analogues, as well as to rationalize the experimental reactivity trends, we carried out a comprehensive mechanistic analysis by combining photophysical and spectroscopic measurements with theoretical DFT calculations and additional photocatalytic experiments.

3.1. Probing the role of excited states in MOF-545: absence of linker-to-metal charge transfer. To evaluate the possibility of a long-lived charged separated state formation in MOF-545-based catalysts and its potential role in the catalytic mechanism, we conducted a photophysical characterization of the catalytic materials by means of time-resolved emission and transient absorption (TA) spectroscopic measurements. Importantly, TA spectroscopy can provide a spectral map of *all* photogenerated states and was thus used here to probe the formation of putative charge-separated species such as oxidized porphyrin linkers and reduced Zr₆ clusters. To this end, we selected the unmetalated MOF-545 and its Zn-metalated analogue, which were studied in DMF solvent due to the stability of the resulting suspension and its suitability for TA measurements. It is important to note that Fe^{III}Cl-TCPP and thus, MOF-545(Fe) could not be investigated with TA spectroscopy, as they are non-emissive due to ultrafast intersystem crossing from a ligand π^* excited state to a low-lying metal-centred ⁴d-d* state, which ultimately relaxes back down to its ground state non-radiatively on a sub-ns timescale.⁴²⁻⁴⁴ All spectral and photophysical features of both MOF-545 and MOF-545(Zn) and their parent linkers TCP and

ARTICLE

Table 1. Photophysical data of MOF-545 and MOF-545(Zn) suspensions.

Sample	³ T excited state absorption lifetimes				³ T ground state bleach lifetimes			
	τ_1 (μ s)	τ_2 (μ s)	A ₁ (%)	A ₂ (%)	τ_1 (μ s)	τ_2 (μ s)	A ₁ (%)	A ₂ (%)
MOF-545	16 ± 3	160 ± 30	29 ± 4%	71 ± 4%	11 ± 2	170 ± 20	46 ± 8%	54 ± 8%
MOF-545(Zn)	5 ± 2	90 ± 20	61 ± 2%	39 ± 2%	10 ± 4	100 ± 20	74 ± 3%	26 ± 3%

**Figure 3.** a) Steady-state transient absorption spectrum of MOF-545(Zn) in DMF using NH₂-bisterminated 1500 M_n PEG as a suspension stabilizer; b) Absorption kinetics of MOF-545(Zn) probed at the excited-state absorption, 480 nm (blue), and the ground-state bleach, 450 nm (green). λ_{exc} = 422 nm, 2-3 mJ/pulse.

(Zn)TCPP in solution may be found in Supplementary Information (Figures S9-S30). Upon laser excitation at the maximum absorption wavelength (λ_{exc} = 422 nm, see Figure 3), MOF-545(Zn) exhibited a ground-state bleach (GSB) at 450 nm and an excited-state absorption (ESA) at 480 nm (Figure 3a). Similarly, MOF-545 displayed a GSB at 430 nm and an ESA at 460 nm (Figure S26). Table 1 compiles the ESA and GSB lifetimes obtained for MOF-545 and MOF-545(Zn) from the fitting of their respective decay and recovery traces to a biexponential model. The biexponential nature of these curves is consistent with the coexistence of two types of porphyrin linkers in our samples.^{30,45} Specifically, the short lifetime (τ_1) in MOF-545 can be ascribed to a small population of N-protonated TCPP linkers, while that of MOF-545(Zn) was attributed to the N-ligation of peripheral Zn centres with the suspension-stabilizer used in our TA experiments (NH₂-PEG-NH₂, 1500 M_n), as evidenced by control experiments of (Zn)TCPP and the stabilizer in solution (see SI for further details). The long lifetime components (τ_2) correspond to the native TCPP and (Zn)TCPP linkers in MOF-545 and MOF-545(Zn), respectively.

Notably, the lifetimes measured at the triplet ESA are consistent with those measured at the GSB for both systems (see Table 1, Figure 3b, and Figures S27-S28), which demon-

strates that the absorbing species (putatively the porphyrin triplet state) decays back to the ground state without the formation of any additional excited state. Most importantly, this finding rules out the formation of charge-separated states via photo-induced electron transfer from the TCPP linkers to the Zr₆ clusters. More specifically, if a charge-separated state was formed, the lifetimes of the ESA and GSB would not agree due to the additional contribution of long-lived oxidized porphyrins in the spectral region of the GSB. Along the same line, several groups proved the lack of efficient linker-to-metal charge-transfer (LMCT) in UiO-66-NH₂ by means of TA, Electron Paramagnetic Resonance (EPR) and DFT.⁴⁶⁻⁴⁸ In fact, as shown in Figures S9-30, the spectral and photophysical features of both analysed MOF-545 and MOF-545(Zn) align quite well with those of their parent linkers in solution, further supporting that Zr₆ clusters are indeed not involved in the excited states of the MOFs formed upon visible-light irradiation. Moreover, in line with these results, time-dependent DFT (TD-DFT) calculations on Zr₆-(TM)TCPP cluster models extracted from MOF-545(TM) structures predicted that the electronic transitions in the visible range involve exclusively the frontier molecular orbitals (MOs), which are centred on the porphyrinic linkers (Figures S31-S32 and Table S5). Notably, empty d(Zr) orbitals of the Zr₆ node lie ≥ 1.5 eV above the LUMO, (Figure S31) rendering any charge-transfer state inaccessible in energy. Overall, the above results allowed ruling out the occurrence of LMCT in unmetalated or metalated MOF-545 upon illumination, and in turn, the participation of a Zr^{III} species in the reaction mechanism.

3.2. Evidence for the photooxidation of TEOA by the porphyrinic linkers of the MOF. To investigate the photochemical processes that MOF-545 (unmetalated, Zn and Fe) may undergo under experimental conditions, steady-state photolysis of the MOF suspensions was carried out in CH₃CN/TEOA (10:1) solutions under an inert atmosphere, using a 350 W Xe-arc lamp equipped with both a 395 nm cut-off and water IR filters (Figure 4). As shown in Figure 4a, long-time exposure of the unmetalated MOF-545 to light resulted in significant changes in the electronic absorption spectrum, with decreased extinction coefficients and small bathochromic

ARTICLE

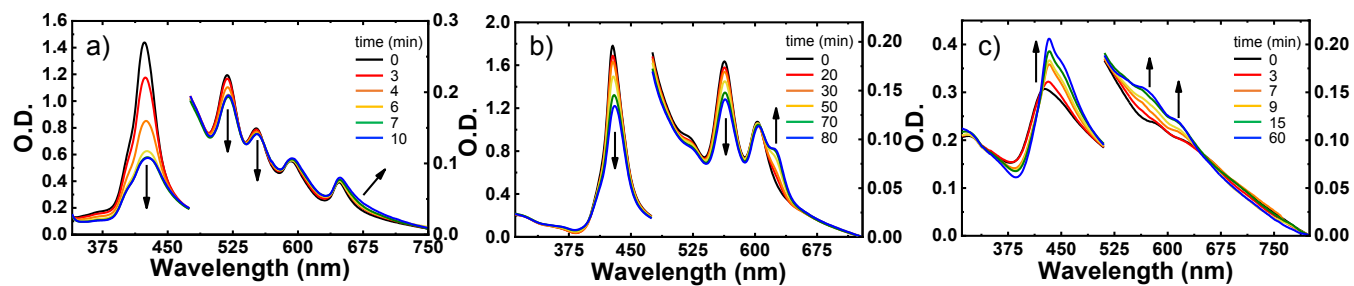


Figure 4. Evolution of the steady-state absorption spectra of: a) MOF-545; b) MOF-545(Zn); and c) MOF-545(Fe^{III}) suspensions in CH₃CN/TEOA (10:1) under an inert atmosphere at increasing irradiation times (black to blue lines) with a 350W Xe arc lamp.

shifts in the Q-bands. These changes reveal the formation of a $2\text{H}^+/2\text{e}^-$ -reduced porphyrin through the protonation across the pyrrolic methine group, known as chlorin.^{49–55} Similar behaviour was observed for the Zn-containing analogue (Figure 4b). In contrast, upon photolysis, while the absorption spectrum of MOF-545(Fe) exhibits a bathochromic shift of the Soret band by 6 nm, an hypsochromic shift of the Q-bands from 586 nm and 628 nm to 572 nm and 614 nm, respectively, was observed (Figure 4c). In addition, the extinction coefficient increased over time for both the Soret and Q-band excitations.^{56–58} It is well-known that these spectral changes (Soret and Q band shift along with increased extinction coefficients) are consistent with the reduction of MOF-545-Fe^{III} to MOF-545-Fe^{II} upon irradiation.^{59–61} Of note, the Soret band splits upon photoreduction with a main peak at 433 nm and a shoulder at 454 nm, which can be attributed to metal ligation resulting in solvent-bound Fe^{II} (433 nm) and TEOA-bound Fe^{II} (454 nm).⁶² The slight broadening of the Soret band is known to be caused by axial ligation of Fe with coordinating solvents and nitrogenous bases.^{61,63–67}

These results indicate that under light irradiation, electrons are transferred from TEOA to the photogenerated holes in the porphyrinic linkers of the MOF. In fact, the photo-oxidation of trialkylamines by (metallo)porphyrins in homogeneous conditions is a well-known process^{59,60} involving the formation of a positively charged aminyl radical (TEOA^{•+}), corresponding to a one-electron oxidised TEOA, in addition to a reduced (metallo)porphyrin. In porphyrins containing a high-valent metal ions, the first reduction is metal-centred, which is what we observed for MOF-545(Fe) (*vide supra*), while in free-base and TM^{II}-containing porphyrins, extra electrons are accommodated in π^* orbitals of the organic framework, leading to (TM^{II})-TCPP^{•-} radical anions (Scheme 1a).⁶⁸ As shown in Scheme 1b, the photogenerated TEOA^{•+} is spontaneously deprotonated by another TEOA molecule to give a neutral TEOA[•] radical species,^{69–71} which we show is stabilised via the formation of a complex with an acetonitrile solvent molecule (Scheme 1c). Notably, the deprotonation of TEOA^{•+} prevents back electron transfer, as the reduction of TEOA[•] is not energetically accessible to Fe^{II}TCPP nor to TM^{II}-containing or unmetalated TCPP^{•-} ($\Delta G > 30 \text{ kcal mol}^{-1}$).

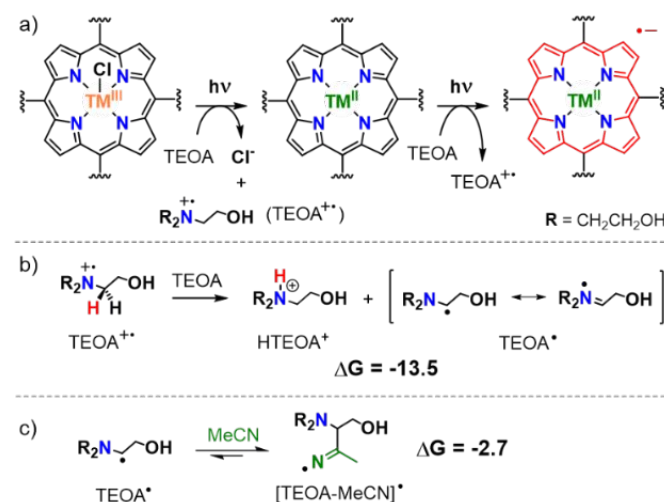
Intriguingly, throughout the photo-oxidation of TEOA by these porphyrinic MOFs, there was no direct spectral evidence of TCPP^{•-} or (Zn)TCPP^{•-} formation, as the typical signatures of the electrochemically-generated TCPP (i.e., a split Soret band and red-shifted Q-bands extending into the NIR region), were not observed.³⁶ However, we clearly observed the formation of (Fe^{II})TCPP species and that of over-reduction products (chlorin species). This indicates that while TCPP linkers can successfully photo-oxidise TEOA upon irradiation, the TCPP^{•-} intermediate is most likely not stable in the framework over extended periods.

At this stage, it is important to note that although the porphyrinic linkers of the metalated (or unmetalated) MOFs are reduced under photocatalytic conditions, they are unlikely to act here as catalytic sites, in contrast with other porphyrin-containing MOFs.^{22,24} To substantiate this, we rely also on the

fact that CO₂ is reduced to formate rather than CO either when using the unmetalated MOF-545 as the catalyst²⁵ or even with other MOFs such as NNU-28,⁷² PCN-136⁷³ and the aminated UiO-66,²¹ which are built on the same Zr-oxo cluster but lack metal centres in their linkers. In addition, the CO₂RR activity of Fe-containing porphyrins has been assigned to a formal Fe⁰ species, which corresponds to a Fe(II) complex with two extra electrons delocalized over the porphyrin framework.⁶⁸ However, we did not observe the formation of such a highly reduced species in our photolysis experiments (Figure 4c). The non-participation of a putative metal-hydride in the reaction mechanism is also supported by the lack of H₂ by-product. Instead, the joint analysis of the preceding works rather suggests that the Zr-oxo clusters are involved in the CO₂RR mechanism. Still, we infer from our above transient spectroscopy and TD-DFT results that such mechanism does not involve the formation of a Zr^{III} species (*vide supra*). Additional TD-DFT calculations showed that charge-separated states are neither accessible under visible-light in a system containing transient TCPP^{•-} linkers (Figure S33).

3.3. Thermally-activated hydrogenation of CO₂ at the Zr₆ nodes. With the above gained knowledge on the photochemical and photophysical properties of the MOF-545(TM) series of catalysts, we next conducted DFT calculations to provide atomistic insights into the reaction mechanism governing the reduction of CO₂ into formate. Specifically, these allowed us to propose and characterise a new reaction mechanism for the thermally-activated hydrogenation of CO₂ to formic acid occurring at the Zr^{IV}₆ nodes of MOF-545 and MOF-545(TM). Figure 5 represents the calculated Gibbs free-energy profile for the herein proposed mechanism, which consists of three main steps: i) the coordination of CO₂ to the Zr₆ cluster; ii) the hydrogenation of CO₂; and iii) the release of the product.

Scheme 1. Photochemical TEOA oxidation by the (TM)TCPP linkers under visible-light illumination and chemical evolution of the one-electron oxidized donor. DFT-derived Gibbs free energies are given in kcal mol⁻¹. The transient TCPP^{•-} radical is highlighted in red.



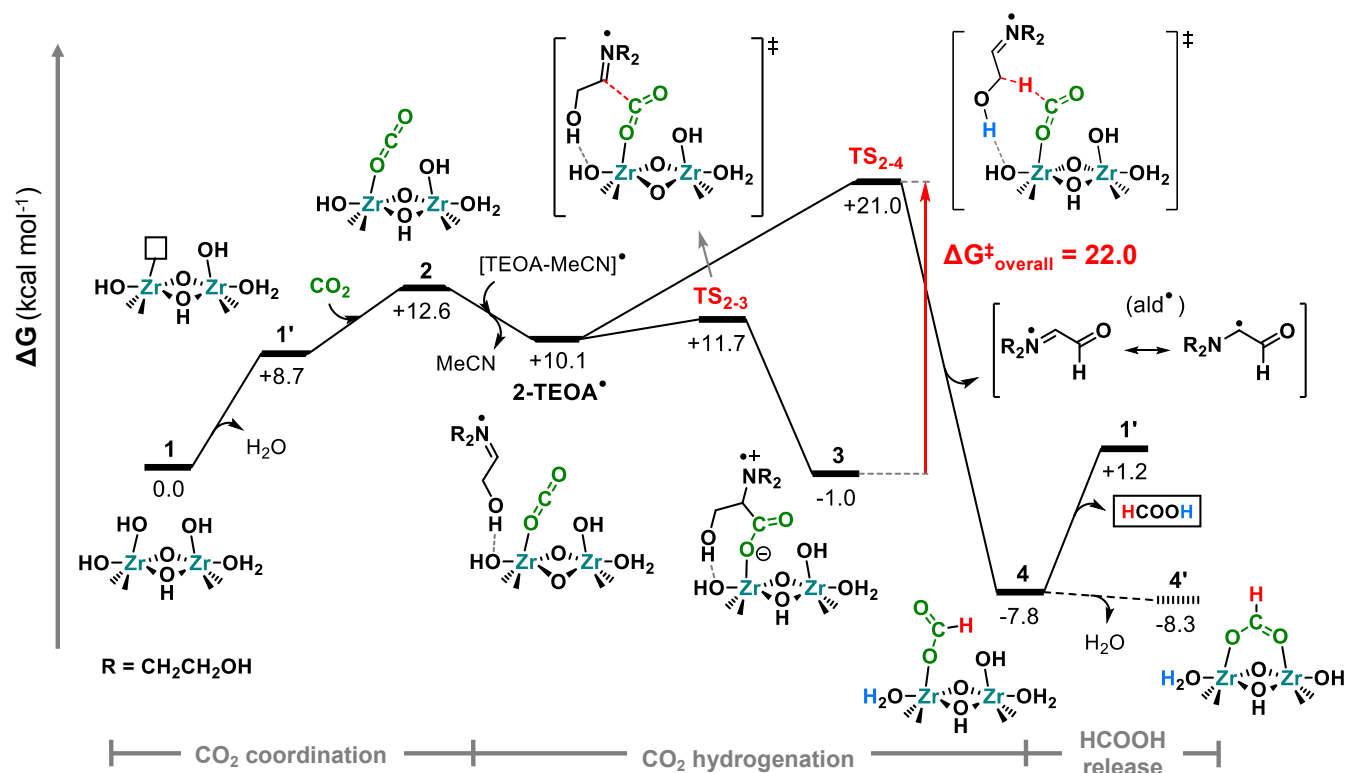


Figure 5. Gibbs free-energy profile (kcal mol⁻¹) for the reduction of CO₂ to formate catalyzed by MOF-545. The red arrow highlights the overall free-energy barrier (3→TS_{2,4}). Relative energies of species that contain a TEOA[•] fragment account for the energy penalty of 2.7 kcal mol⁻¹ associated to displacing the equilibrium depicted in Scheme 1c towards the free reducing agent in solution. The free-energy cost for the product release considers the product as a non-covalent formate...TEOA adduct in solution (see Figure S40).

Following the photo-oxidation of TEOA at the porphyrinic linkers (vide supra), the hydrogenation of CO₂ requires the substitution of a labile aqua ligand from the Zr₆ cluster (1) by a CO₂ molecule, which binds to Zr^{IV} ion through one oxygen atom giving species 2. This stepwise process proceeds uphill and is endergonic by 12.6 kcal mol⁻¹ (Figure 5). In species 2, the C=O(Zr) bond of CO₂ is polarised by the effect of the Zr^{IV} ion acting as a Lewis acid, increasing the electrophilicity of the carbon atom, *i.e.* activating it for a nucleophilic attack. As such, we found that photogenerated TEOA[•] radicals (see Scheme 1) can perform a nucleophilic attack on the C atom of a Zr-bound CO₂ through TS_{2,3} (represented in Figure 6a), overcoming a very small free-energy barrier of 1.6 kcal mol⁻¹ from the 2-TEOA[•] non-covalent adduct. This process leads to intermediate 3, where a C-C bond is formed between the Zr-O=C=O group and the alpha carbon of TEOA[•]. This species is surprisingly stable, laying 1 kcal mol⁻¹ below the reactants in terms of free energy. This was ascribed to its zwitterionic nature whereby both positive and negative charges are stabilised by the electron-donating character of the alkyl chains and the electron-withdrawing character the Zr^{IV} centre, respectively (Figure S35). The lifetime of free TEOA[•] radicals has been reported to be of a few ms in aqueous solutions,⁷⁴ which translates into degradation barriers of ca. 14 kcal mol⁻¹ assuming first-order kinetics, most likely due to its high tendency to undergo oxidation processes (E_{ox} of -1.12 V vs SCE).⁷⁵ However, the formation of 3 through a kinetically accessible pathway

stabilises the SOMO of TEOA[•] by 3.3 eV, hampering its oxidation and in turn, preventing its decomposition.

From 3, TEOA[•] can be regenerated by going back to the 2-TEOA[•] adduct through TS_{2,3}, ($\Delta G^\ddagger = 12.7$ kcal mol⁻¹, see Figure 5). Interestingly, our DFT calculations revealed that once released, TEOA[•] can transfer a formal hydride (highlighted in red in Figure 5) to the carbon atom of the Zr^{IV}-bound CO₂ through a smooth free-energy barrier of 10.9 kcal mol⁻¹ involving TS_{2,4} (shown in Figure 6b). This hydride-transfer triggers the spontaneous abstraction of the hydroxyl proton of TEOA[•] (highlighted in blue) by a basic Zr-OH site of the MOF to form a Zr-bound aqua ligand (see Figures S37-S38 and SI text for details), releasing an aldehyde-like radical (ald[•]). This concerted asynchronous process yields species 4, in which the formate product remains attached to the Zr₆ cluster and confers an irreversible character to the reaction, with a reverse free-energy barrier of 28.8 kcal mol⁻¹. Note that with a lifetime in the ms time scale, TEOA[•] is expected to live long enough to hydrogenate a Zr-bound CO₂ in acetonitrile through a barrier of ca. 11 kcal mol⁻¹ (from 2-TEOA[•] to TS_{2,4}). For comparison, the hydride-transfer from TEOA[•] to a non-activated CO₂ accounts for a free-energy barrier of 25 kcal mol⁻¹ (Figure S39), being 14.1 kcal mol⁻¹ higher than that assisted by Zr₆, which evidences the positive influence of the Zr^{IV} ion acting as a Lewis acid.

Very recently, several unusual roles have been reported to be played by TEOA in the photoreduction of CO₂ by Ru-based molecular catalysts.⁷⁶ However, this is to our knowledge the

first time that the neutral TEOA[•] radical involved in the decomposition of TEOA upon photooxidation is proposed to act as a 2e⁻/2H⁺ *reducing species* that transfers a nucleophilic hydride to a Lewis-acid activated CO₂ molecule. In this process, the initial oxidation of TEOA is strictly required to create reactive allylic protons near a heteroatom. Such a pattern facilitates the hydride-transfer by delocalizing the positive charge generated in the process, as recently observed for structurally similar allylic alcohols capable of transferring a hydride to an electrophilic Ti^{IV}-hydroperoxo group.⁷⁷

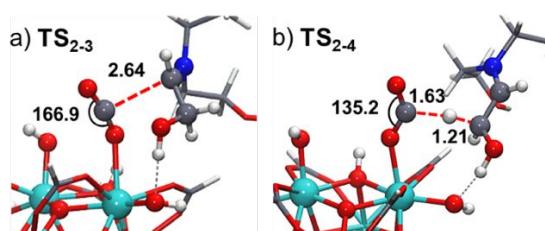


Figure 6. Balls-and-sticks representations of the DFT-optimized geometries for **TS_{2,3}** (a) and **TS_{2,4}** (b). Main distances and angles are given in Å and degrees, respectively. See SI for spin density distributions (Figures S34 and S36) and detailed description of the nature of these processes.

Finally, the release of the formic acid product from species **4** to regenerate **1'** is endergonic by 9 kcal mol⁻¹, in agreement with the experimental observations reporting the strong adsorption of the product in MOF-545 (*vide supra*). It is worth noting that upon releasing an aqua ligand, species **4** may also evolve to the slightly more stable **4'** where the formate anion coordinates two neighbouring Zr ions in a bridged fashion (see Figure 5). The fate of the aldehyde-like radical species (ald[•]) formed after **TS_{2,4}** might be that of being reductively quenched by a reduced porphyrin linker and protonated by HTEOA⁺ (see Scheme S2) yielding an aldehyde by-product (ald), previously reported as a photo-degradation product of TEOA.⁷¹ In fact, its formation was indeed confirmed in the present work by the analysis of the reaction mixture after the photocatalytic tests described above with ¹H NMR and mass spectrometry (Figures S41-S45), thus supporting the proposed mechanism. Alternative mechanisms involving the formation of a Zr hydride assisted by TEOA[•] or sequential electron-transfer + proton transfer pathways were found to be less favourable (see SI for details).

Overall, being slightly more stable than the reactant, species **3** is expected to act as the resting state of the catalytic cycle governing the thermal CO₂-reduction step. Thus, the overall free-energy barrier (**3**→**TS_{2,4}**, highlighted with a red arrow in Figure 5) accounts for a moderate value of 22.0 kcal mol⁻¹, which can be easily overcome at room temperature. Even so, and due to the computed small energy differences (Figure S46), it cannot be discarded that species **4** (or **4'**) in subsequent cycles could represent the catalyst resting state due to an increased concentration of formic acid in solution.

4. Validation of the proposed reaction mechanism.

Next, we carried out a series of additional photocatalytic experiments in order to test the respective roles of TEOA and of the porphyrins as proposed in our mechanistic investigation. First, we performed a new set of catalytic tests with the free-base MOF-545 in the presence of an additional amount of molecular Fe^{III}Cl-TCPPOMe (TCPPOMe = tetramethoxyphenylporphyrin) added in solution allowing a ~1:1 ratio between porphyrins in solution and in the MOF. The choice of Fe^{III}Cl-TCPPOMe was guided by the fact that MOF-545(Fe) yields the highest formate production among the MOF-545(TM) materials investigated herein. Besides, the ester form of the porphyrin was used for solubility reasons. Having the proposed mechanism in mind, the iron-porphyrin added in solution is meant to act as an auxiliary TEOA photo-oxidation agent. It is thus expected to boost the concentration of the TEOA[•] and in turn, accelerate the rate of CO₂RR. Figure 7 shows that indeed, the addition of the iron-porphyrin in solution increases the yield of formate produced by the free-base MOF-545 by a factor of 1.75 (see Figure 7). This enhancement (purple contribution, Figure 7) cannot be only ascribed to the small catalytic activity of the molecular iron-porphyrin added in solution, since the {MOF-545, Fe^{III}Cl-TCPPOMe} system produces much more formate (175%) than the combination of the individual MOF-545 (100%) and Fe^{III}Cl-TCPPOMe (25%) systems do. This suggests the expected boost in the concentration of TEOA[•], which accelerates the production of formate catalyzed by the MOF.

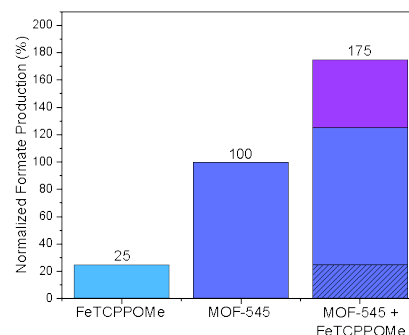


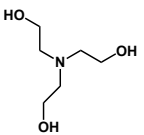
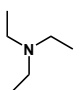
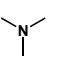
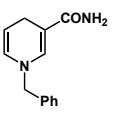
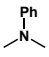
Figure 7. Formate production upon CO₂ reduction with Fe-TCPPOMe (1.2 mg) and/or free-base MOF-545 (2 mg) allowing a ~1:1 ratio between porphyrins in solution and in the MOF. Experiments were conducted in 2 mL CH₃CN/TEOA (10:1) for 4h under 280 W Xenon lamp (λ > 415 nm). The amount of formate detected was normalized with respect to that of MOF-545 corresponding to 100% activity.

Complementary experiments were performed whereby the radical scavenger, 5,5-dimethyl-1-pyrroline-N-oxide (DMPO), was added in the photocatalytic experiments in order to inhibit the formation of radicals, such as TEOA[•], TEOA^{••+} or TCPP^{•-} mentioned above. Notably, a substantial drop of ~70% in the photocatalytic activity of the MOF-545(Fe) was observed upon addition of DMPO (Figure S47), confirming explicitly the essential role of such radicals in the photocatalytic reduction of CO₂ into formate.

In addition, a series of photocatalytic experiments were conducted to evaluate the impact of the nature of the sacrificial electron/proton donor in the CO₂RR photocatalytic activity of

NanoMOF-545(Fe). Table 2 compares the formate yield obtained with TEOA with those obtained with other sacrificial donors commonly used in the literature.⁷¹ These include triethylamine (TEA), trimethylamine (TMA), benzyl-dihydronicotinamide (BNAH) and dimethylaniline (DMA). Remarkably, the highest formate production was reported with TEOA, being ca. 10-fold lower with TEA and TMA, and zero with BNAH and DMA. This is quite noteworthy because TEOA is the weakest electron donor of all the series, displaying the lowest-lying HOMO among the series of donors. This indicates that a more efficient reduction of the MOF using a more reducing sacrificial donor does not lead to a higher catalytic activity. Conversely, we found that the formate production is directly proportional to the computed hydricity of the photogenerated radical species - whereby the lower the value, the higher the hydricity (Table 2, column 4) - further supporting the role of TEOA[•] as hydride donor. Indeed, we noticed that most of the experimental works that reported the formation of formate with Zr-based porphyrinic MOFs also employed TEOA as sacrificial donor (Table S2). Other works performed the catalytic experiments in the presence of other aliphatic alcohols structurally similar to TEOA that might display analogous reactivity, such as ethylene glycol²⁷ or triisopropanolamine.⁷³

Table 2. Comparison of the properties and performances of different electron/proton donors for the photocatalytic CO₂RR promoted by NanoMOF-545(Fe).^a

Donor	Structure	E _{HOMO} (eV)	Radical hydricity (kcal mol ⁻¹) ^b	HCOO ⁻ yield (%)
TEOA		-8.01	+66.1	100
TEA		-7.84	+79.2	11.6
TMA		-7.95	+89.6	8.3
BNAH		-7.08	^c	0
DMA		-7.14	+96.8	0 ^d

^a Conditions: 2 mg of catalyst in 10:1 CH₃CN:Donor solution after degassing with pure CO₂ for 20 min. Formate was quantified by ionic chromatography (IC) after 4h irradiation (λ > 415 nm, 280 W). ^b Hydricity computed as the standard free-energy change associated to the process: D[•] → D^{•+} + H⁻. Thus, the lower the value, the higher the hydricity. ^c Radical with no β-protons suitable for hydride transfer. ^d The MOF was not stable in CH₃CN:DMA solution, no formate was quantified by IC.

5. Explaining the photocatalytic activity trends along the series of MOF-545(TM) catalysts.

Finally, taking advantage of the acquired knowledge on the reaction mechanism, we aimed at rationalizing the

experimental reactivity trends observed upon varying the nature of the linker in the MOF-545-based catalyst (Figure 2). As the metalation of the MOF's linker is not expected to alter the Lewis acidity of the Zr^{IV} ions of the nodes, we hypothesized that the variation of photocatalytic performances observed along the series of MOF-545(TM) catalysts might emanate from their different ability of the metalated porphyrinic linkers to promote the photo-oxidation of TEOA, required to provide the key TEOA[•] species capable of hydrogenating CO₂. As shown in Figure S31, the frontier molecular orbitals of the free-base TCPP linkers are aligned with those of TM^{II}-containing metalated linkers, thus exhibiting similar oxidizing power. We thus considered that the CO₂RR photocatalytic performance of a metalated MOF might be correlated to the ability of the metal ion of the TCPP linkers to coordinate TEOA through its N atom. Such coordination would allow the photooxidation of TEOA to take place through an inner-sphere electron transfer mechanism, which is expected to be faster and more efficient than the outer-sphere electron transfer mechanism governing the photo-oxidation of TEOA in the free-base linker. In fact, we determined via titration experiments that TEOA spontaneously binds to Zn^{II}-TCPP, with a binding constant of ~5 M⁻¹ in DMF (Figures S48, S49).

Consistently with the above hypothesis, the highest photocatalytic activities among the MOF-545(TM) series are observed for those containing TM^{III} metals centers, such as MOF-545(Mn) and MOF-545(Fe), these being more prone to accept electrons from TEOA than their TM^{II}-containing analogues due to the lower-energy lying nature of their frontier MOs (Figure S31). Interestingly, while being less electronically inclined to accept electrons than TM^{III}-containing MOFs, MOF-545(Zn) displays a photocatalytic activity comparable to that of MOF-545(Mn), outperforming the rest of TM^{II}-containing samples. This can be rationalized on the basis of the superior light-harvesting properties of Zn-TCPP as compared to other TM^{II}-TCPPs,⁷⁸⁻⁸⁰ combined with its ability to bind TEOA that ensures a highly efficient TEOA photo-oxidation process. Moreover, titration experiments revealed that the binding constant of TEOA to Fe^{III}Cl-TCPP (~10⁵ M⁻¹ in DMF), is several orders of magnitude higher than that to Zn^{II}-TCPP (~5 M⁻¹) (Figures S50, S51), further explaining the higher activity reported for the MOF-545(Fe) catalyst.

Conclusions

By combining experimental and computational techniques, we have elucidated with atomistic detail the complex reaction mechanism responsible for the photocatalytic reduction of CO₂ to formate catalyzed by Zr-based porphyrinic MOF-545 catalysts in CH₃CN/TEOA (10:1) solutions, while exploring two complementary strategies to boost the photocatalytic activity of the material. These include the systematic metalation of the porphyrinic linkers of the MOF to yield an entire series of MOF-545(TM) catalysts, and the synthesis of the MOF-545(Fe) as nanosized particles. All the prepared catalysts showed 100 % selectivity towards formate production and the yield increases with TM = free base ≈ Cu^{II} < Co^{II} < Mn^{III} ≤ Zn^{II} < Fe^{III}, reaching 2264 μmol g⁻¹ after 4 h with MOF-545(Fe). The photocatalytic

activity of MOF-545(TM)-based nanocrystals (~150 nm length) is significantly boosted with respect to the conventional micron-sized crystals due to an increased density of solvent-accessible catalytic sites. This strategy allowed a remarkable maximum formate production of 6000 $\mu\text{mol g}^{-1}$ after 4 h with MOF-545(Fe), being one of the highest productions of formate amongst MOF catalysts reported to date.

By combining spectroscopic, photophysical and computational techniques we have evidenced a new reaction mechanism for the photocatalytic reduction of CO_2 to formate promoted by MOF-545(TM) catalytic materials, which is summarized in Figure 8. This consists of three main processes: i) the photooxidation of TEOA at the porphyrinic linkers of the MOF to yield TEOA $^{\bullet}$ radicals upon deprotonation of the as-generated TEOA $^{\bullet+}$; ii) the thermally-activated reduction of CO_2 catalysed by the Zr_6 Lewis acid nodes, whereby TEOA $^{\bullet}$ unprecedently serves as a *hydride-donor* species; and iii) the termination via radical quenching between reduced linkers (TCPP $^{\bullet-}$) and the dehydrogenated donor (ald $^{\bullet}$). Importantly, photophysical studies of MOF-545 and MOF-545(TM), supplemented by TD-DFT calculations ruled out the possibility of photo-induced linker-to-metal charge transfer leading to charge separated states suitable for subsequent CO_2 RR. This proposed mechanism was further validated by additional photocatalytic experiments and allowed explaining the experimental activity trends on the basis of the ability of the porphyrinic linker to promote the photooxidation of TEOA under visible-light irradiation.

Overall, these findings represent a step forward towards understanding the catalytic processes that make use of photosensitive materials in combination with TEOA (or structurally similar) electron/proton donors and is expected to inspire the design of new multi-component catalytic platforms for photo-reduction reactions with improved activity and selectivity.

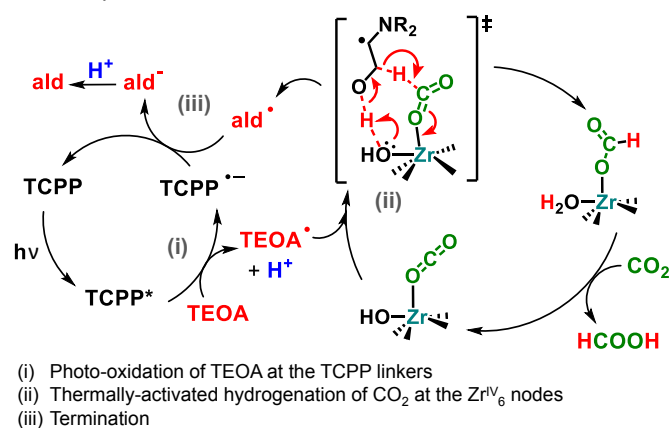


Figure 8. Schematic summary of the proposed reaction mechanism for the photocatalytic reduction of CO_2 to formic acid with TEOA promoted by Zr-based porphyrinic MOFs. $\text{R} = \text{CH}_2\text{CH}_2\text{OH}$.

Experimental Section

NanoMOF-545 synthesis. 137 mg (0.425 mmol) of $\text{ZrOCl}_2 \cdot 8\text{H}_2\text{O}$, 30 mg (0.038 mmol) of TCPP and 300 μL of 1,2-dichloroacetic acid were dissolved in 10 mL DMF in a 100 mL Teflon vial. The

mixture was heated for 20 min under microwave (150 $^{\circ}\text{C}$, 800 W) with vigorous stirring. After cooling to room temperature, a powder was collected by centrifugation. The MOF was then heated at 130 $^{\circ}\text{C}$ for two hours in a 10 mL DMF / 1 mL 1M HCl mixture. After centrifugation, the obtained material was rinsed twice with DMF and twice with acetone. Lastly, the powder was dispersed in 20 mL of acetone and stirred overnight. The final compound was collected by centrifugation, rinsed twice with acetone and then dried at 100 $^{\circ}\text{C}$ ($m = 28$ mg, yield 56% based on TCPP).

NanoMOF-545(Fe) synthesis. 137 mg (0.425 mmol) of $\text{ZrOCl}_2 \cdot 8\text{H}_2\text{O}$, 32 mg (0.036 mmol) of (Fe)TCPP and 900 μL of 1,2-dichloroacetic acid were dissolved in 30 mL DMF in a 100 mL Teflon vial. The mixture was heated for 20 min under microwave (150 $^{\circ}\text{C}$, 800 W) with vigorous stirring. After cooling to room temperature, a powder was collected by centrifugation. The MOF was then heated at 130 $^{\circ}\text{C}$ for two hours in a 30 mL DMF / 3 mL 1M HCl mixture. After centrifugation, the obtained material was rinsed twice with DMF and twice with acetone. Lastly, the powder was dispersed in 20 mL of acetone and stirred overnight. The final compound was collected by centrifugation and rinsed twice with acetone then dried at 100 $^{\circ}\text{C}$ ($m = 30$ mg, yield 61% based on (Fe)TCPP). EDX calcd. (exp.): Fe/Zr 0.33 (0.32).

Photocatalysis experiments. 2 mg of catalyst and 2 mL of a $\text{CH}_3\text{CN}/\text{TEOA}$ (10:1) mixture were added to a 4 mL sealed quartz cuvette and sonicated for 10 min. The cuvette was then submitted to a CO_2 flux for 20 min before being irradiated for 4 h with a 280 W Xenon lamp (Newport) equipped with a 415 nm UV cut-off glass filter (Newport) and a temperature-controlled block at 20 $^{\circ}\text{C}$. Gas products were analysed via gas chromatography while liquid products were assessed by ionic chromatography (IC). After the catalytic process, the catalyst was recollected by centrifugation, dispersed in 2 mL of milli-Q water and stirred at 60 $^{\circ}\text{C}$ for 1 h. An aliquot of the liquid phase was collected and analysed by IC to quantify the remaining formate leached by the MOF.

Steady-state photoreduction sample preparation. Prior to photoreduction experiments, approximately 0.5-1 mg of MOF-545, MOF-545(Zn) or MOF-545(Fe) was added to a 6-dram vial and suspended with a $\text{CH}_3\text{CN}/\text{TEOA}$ (10:1) solution. The vial contents were then sonicated for 1-2 min and transferred to a custom optical cell (Quark Glass, 1.0 cm pathlength), with a female 24/40 joint. A stir bar was added to the optical cell and a rubber septum was used to seal the joint. The suspension was then degassed with Ar gas for 20-30 min away from light. Afterwards, the rubber septum was wrapped a few times with parafilm to prevent air leakage. The solution-state preparations followed the same protocol, with the only difference being the solvent matrix. For TCPP and (Zn)TCPP, a 10:1 DMF/TEOA matrix was used to dissolve the solids, whereas the FeTCPPCl sample was able to reasonably dissolve with $\text{CH}_3\text{CN}/\text{TEOA}$ (10:1).

Steady-State photoreduction measurements. The photoreduction measurements were performed with a 350 W Xe arc lamp (Newport, SP66921-5513) using a water IR filter (Newport, 6123NS) and a 395-nm cut-on glass filter (Newport, FSQ-GG395). The samples were stirred approximately 2 ft from the arc lamp lens. At each time interval (1-10 min), the sample was removed from stirring and placed in the sample chamber of a Cary 5000 UV-Vis-NIR spectrometer (Agilent) to measure the electronic absorption spectrum. After the measurement, the

sample was placed back in from of the arc lamp, where it remained until the next spectral measurement. Measurements were ceased when no spectral changes were observed over three-time intervals.

Steady-State and time-resolved emission measurements. The steady-state emission spectra were obtained using a QuantaMaster Model QM-200-4E emission spectrophotometer from Photon Technology, Inc. (PTI). The excitation light source was a 75 W Xe arc lamp (Newport). The detector was a thermoelectrically cooled Hamamatsu 1527 photomultiplier tube (PMT). Time-resolved fluorescence lifetimes were obtained *via* the time-correlated single photon counting technique (TCSPC) with the same QuantaMaster Model QM-200-4E emission spectrophotometer from Photon Technology, Inc. (PTI) equipped with a 415 nm LED and a Becker & Hickl GmbH PMH-100 PMT detector with time resolution of < 220 ps FWHM. The instrument response function (1.5 ns FWHM) was measured at 415 nm using a dilute suspension of BaSO₄ in water. Kinetic reconvolutions with the instrument response function were fit using the Edinburgh Instruments L900 software suite. All other data was processed in OriginPro.

Sample preparation for transient absorption measurements. Samples were prepared by adding approximately 3 mg of MOF-545 or MOF-545(Zn) and 100 mg of NH₂-terminated polyethylene glycol (2000 M_w PEGNH₂) to a 2-dram vial. Then, 3 mL of anhydrous DMF were added to the vial and the contents were sonicated for 3-5 min. The suspension was then centrifuged at 6800 rpm (IKA mini G centrifuge), for 30 s. The supernatant was transferred into an optical cell and diluted with DMF until it provided an absorbance at or below 2.0. The solutions were then sealed with a rubber septum, degassed with Ar for 20-30 min and then used in the experiments. The errors associated with each measurement are the standard deviations from multiple measurements.

Transient absorption measurements. Steady-state and time-resolved transient absorption measurements were conducted with an Edinburgh Instruments LP980 laser flash photolysis system. The pump source was a frequency doubled (532 nm) Spectra-Physics Quanta-Ray INDI Nd:YAG laser, operating at 1Hz with a 6-8 ns pulse width. The spectrometer was equipped with an Andor i-Star ICCD camera for steady-state measurements and a Hamamatsu R928 PMT for measuring single wavelength kinetics. The white light source was a pulsed 150 W XBO Xe arc lamp. The average energy per pulse was kept at 4mJ. Sample stability was monitored via UV-Vis before and after measurements. For spectral absorption mappings, time-zero was defined as the emission signal after the exciting laser pulse disappeared from the emission spectrum. The reported single-wavelength kinetic lifetimes were averaged over multiple trials.

Computational details. DFT calculations were performed at the ω B97X-D level⁸¹ using the Gaussian 16 (rev. B01) quantum chemistry package.⁸² Main-group elements were treated with a Pople-type 6-31G(d,p) basis set,⁸³⁻⁸⁵ while transition metal centres were described by the LANL2DZ basis set (and associated pseudopotentials)⁸⁶ and supplemented with f-type polarization functions.⁸⁷ Solvent effects of acetonitrile were included in the geometry optimizations and energy calculations by means of the IEF-PCM implicit solvent model,⁸⁸ as implemented in Gaussian 16. The nature of the minima and saddle points on the potential energy surface was confirmed via

frequency calculations. The free energies of all the species were corrected from the reference state of 1 atm to the standard state of 1.0 M in solution at 25 °C (+1.89 kcal mol⁻¹), except for acetonitrile, for which the standard state corresponds to a higher concentration as it acts as solvent in this reaction. Thus, its standard-state correction was calculated according to a density of 0.786 g cm⁻³, which leads to a value of +3.64 kcal mol⁻¹. The catalytic Zr₆ nodes of the MOFs were modelled adopting the most likely protonation pattern, with 4 alternated μ_3 -OH groups in antisymmetric disposition and one hydroxo and one aqua ligand per undercoordinated Zr site.⁸⁹ The chelating linkers were modelled as carboxylic groups capped with H atoms, as previously done by other authors.⁹⁰ The absorption spectra of Zr₆-TCPP and several TCPP(TM) cluster models were simulated by means of time-dependent DFT^{91,92} using the same level of theory described above, whereas additional DFT calculations to analyse in more detail the electronic structure of the material were carried out with the HSE06 functional,⁹³ which has been successfully used to reproduce experimental bandgaps in Zr-MOFs⁹⁴ in combination with the SDD basis set with Stuttgart/Dresden pseudopotentials^{95,96} for metal centres and the 6-31G(d,p) basis set⁸³⁻⁸⁵ for remaining atoms.

Author Contributions

The manuscript was written through contributions of all authors. All authors have given approval of the final version of the manuscript. †Y. B., A. S.-D. and D. R. C. contributed equally.

Conflicts of interest

There are no conflicts to declare.

Acknowledgements

This work was supported by CNRS, UVSQ, the Ministère de l'Enseignement Supérieur, de la Recherche et de l'Innovation, the French National Research Agency (ANR) as part of the "Investissements d'Avenir" program n°ANR-11-IDEX-0003-02 and CHARMMMAT ANR-11-LABX-0039. This work was additionally supported by the U.S. Department of Energy, Office of Science, Office of Basic Energy Sciences, under Award DE-SC0012445. The calculations have been performed using the HPC national resources from GENCI (CINES/TGCC) through Grant 2016-097343. Aurélie Damond and Mathieu Frégnaux are gratefully acknowledged for mass spectrometry and XPS measurements, respectively.

References

- 1 A. Stips, D. Macías, C. Coughlan, E. Garcia-Gorrioz and X. S. Liang, *Sci. Rep.*, 2016, **6**, 21691.
- 2 M. Fajardy, P. Patrizio, H. A. Daggash and N. Mac Dowell, *Front. Clim.*, 2019, **1**, 6.

- 3 J. Artz, T. E. Müller, K. Thenert, J. Kleinekorte, R. Meys, A. Sternberg, A. Bardow and W. Leitner, *Chem. Rev.*, 2018, **118**, 434–504.
- 4 B. M. Tackett, E. Gomez and J. G. Chen, *Nat. Catal.*, 2019, **2**, 381–386.
- 5 G. Takalkar, R. R. Bhosale, F. AlMomani and M. Khraisheh, *Fuel*, 2019, **257**, 115965.
- 6 R. N. Biboum, C. P. N. Njiki, G. Zhang, U. Kortz, P. Mialane, A. Dolbecq, I. M. Mbomekalle, L. Nadjo and B. Keita, *J Mater Chem*, 2011, **21**, 645–650.
- 7 Y.-R. Wang, Q. Huang, C.-T. He, Y. Chen, J. Liu, F.-C. Shen and Y.-Q. Lan, *Nat. Commun.*, 2018, **9**, 4466.
- 8 Y. T. Guntern, J. R. Pankhurst, J. Vávra, M. Mensi, V. Mantella, P. Schouwink and R. Buonsanti, *Angew. Chem. Int. Ed.*, 2019, **58**, 12632–12639.
- 9 C. Cometto, R. Kuriki, L. Chen, K. Maeda, T.-C. Lau, O. Ishitani and M. Robert, *J. Am. Chem. Soc.*, 2018, **140**, 7437–7440.
- 10 S. Wang, M. Xu, T. Peng, C. Zhang, T. Li, I. Hussain, J. Wang and B. Tan, *Nat. Commun.*, 2019, **10**, 676.
- 11 D. C. Grills, J. A. Farrington, B. H. Layne, S. V. Lymar, B. A. Mello, J. M. Preses and J. F. Wishart, *J. Am. Chem. Soc.*, 2014, **136**, 5563–5566.
- 12 V. Kumaravel, J. Bartlett and S. C. Pillai, *ACS Energy Lett.*, 2020, **5**, 486–519.
- 13 D. Yang, H. Yu, T. He, S. Zuo, X. Liu, H. Yang, B. Ni, H. Li, L. Gu, D. Wang and X. Wang, *Nat. Commun.*, 2019, **10**, 3844.
- 14 X. Deng, R. Li, S. Wu, L. Wang, J. Hu, J. Ma, W. Jiang, N. Zhang, X. Zheng, C. Gao, L. Wang, Q. Zhang, J. Zhu and Y. Xiong, *J. Am. Chem. Soc.*, 2019, **141**, 10924–10929.
- 15 A. Efrati, C.-H. Lu, D. Michaeli, R. Nechushtai, S. Alsaoub, W. Schuhmann and I. Willner, *Nat. Energy*, 2016, **1**, 1–8.
- 16 R. K. Singh, R. Singh, D. Sivakumar, S. Kondaveeti, T. Kim, J. Li, B. H. Sung, B.-K. Cho, D. R. Kim, S. C. Kim, V. C. Kalia, Y.-H. P. J. Zhang, H. Zhao, Y. C. Kang and J.-K. Lee, *ACS Catal.*, 2018, **8**, 11085–11093.
- 17 S. R. Lingampalli, M. M. Ayyub and C. N. R. Rao, *ACS Omega*, 2017, **2**, 2740–2748.
- 18 Y.-H. Luo, L.-Z. Dong, J. Liu, S.-L. Li and Y.-Q. Lan, *Coord. Chem. Rev.*, 2019, **390**, 86–126.
- 19 E. Gong, S. Ali, C. B. Hiragond, H. Soo Kim, N. S. Powar, D. Kim, H. Kim and S.-I. In, *Energy Environ. Sci.*, 2022, **15**, 880–937.
- 20 Y. Fu, D. Sun, Y. Chen, R. Huang, Z. Ding, X. Fu and Z. Li, *Angew. Chem. Int. Ed.*, 2012, **51**, 3364–3367.
- 21 D. Sun, Y. Fu, W. Liu, L. Ye, D. Wang, L. Yang, X. Fu and Z. Li, *Chem. – Eur. J.*, 2013, **19**, 14279–14285.
- 22 W. Morris, B. Voloskiy, S. Demir, F. Gándara, P. L. McGrier, H. Furukawa, D. Cascio, J. F. Stoddart and O. M. Yaghi, *Inorg. Chem.*, 2012, **51**, 6443–6445.
- 23 H. Zhang, J. Wei, J. Dong, G. Liu, L. Shi, P. An, G. Zhao, J. Kong, X. Wang, X. Meng, J. Zhang and J. Ye, *Angew. Chem. Int. Ed.*, 2016, **55**, 14310–14314.
- 24 X.-J. Kong, T. He, J. Zhou, C. Zhao, T.-C. Li, X.-Q. Wu, K. Wang and J.-R. Li, *Small*, 2021, **17**, 2005357.
- 25 H.-Q. Xu, J. Hu, D. Wang, Z. Li, Q. Zhang, Y. Luo, S.-H. Yu and H.-L. Jiang, *J. Am. Chem. Soc.*, 2015, **137**, 13440–13443.
- 26 R. Hariri and S. Dehghanpour, *Appl. Organomet. Chem.*, 2021, **35**, e6422.
- 27 J. Jin, *New J. Chem.*, 2020, **44**, 15362–15368.
- 28 W.-Y. Gao, H. T. Ngo, Z. Niu, W. Zhang, Y. Pan, Z. Yang, V. R. Bhethanabotla, B. Joseph, B. Aguila and S. Ma, *ChemSusChem*, 2020, **13**, 6273–6277.
- 29 M. Dan-Hardi, C. Serre, T. Frot, L. Rozes, G. Maurin, C. Sanchez and G. Férey, *J. Am. Chem. Soc.*, 2009, **131**, 10857–10859.
- 30 S. M. Shaikh, A. Chakraborty, J. Alatis, M. Cai, E. Danilov and A. J. Morris, *Faraday Discuss.*, 2019, **216**, 174–190.
- 31 M. Kim, J. S. Oh, B. H. Kim, A. Y. Kim, K. C. Park, J. Mun, G. Gupta and C. Y. Lee, *Inorg. Chem.*, 2020, **59**, 12947–12953.
- 32 P. Deria, J. Yu, R. P. Balaraman, J. Mashni and S. N. White, *Chem. Commun.*, 2016, **52**, 13031–13034.
- 33 X. Li, J. Yu, D. J. Gosztola, H. C. Fry and P. Deria, *J. Am. Chem. Soc.*, 2019, **141**, 16849–16857.
- 34 S. Choi, W.-J. Jung, K. Park, S.-Y. Kim, J.-O. Baeg, C. H. Kim, H.-J. Son, C. Pac and S. O. Kang, *Acs Appl. Mater. Interfaces*, 2021, **13**, 2710–2722.
- 35 J.-Y. Zeng, X.-S. Wang, B.-R. Xie, Q.-R. Li and X.-Z. Zhang, *J. Am. Chem. Soc.*, 2022, **144**, 1218–1231.
- 36 J. Liu, Y.-Z. Fan, X. Li, Z. Wei, Y.-W. Xu, L. Zhang and C.-Y. Su, *Appl. Catal. B Environ.*, 2018, **231**, 173–181.
- 37 M. B. Majewski, H. Noh, T. Islamoglu and O. K. Farha, *J. Mater. Chem. A*, 2018, **6**, 7338–7350.
- 38 G. Paille, M. Gomez-Mingot, C. Roch-Marchal, B. Lassalle-Kaiser, P. Mialane, M. Fontecave, C. Mellot-Draznieks and A. Dolbecq, *J. Am. Chem. Soc.*, 2018, **140**, 3613–3618.
- 39 M. L. Kelty, W. Morris, A. T. Gallagher, J. S. Anderson, K. A. Brown, C. A. Mirkin and T. D. Harris, *Chem. Commun.*, 2016, **52**, 7854–7857.
- 40 B. L. Bonnett, E. D. Smith, M. De La Garza, M. Cai, J. V. Haag, J. M. Serrano, H. D. Cornell, B. Gibbons, S. M. Martin and A. J. Morris, *ACS Appl. Mater. Interfaces*, 2020, **12**, 15765–15773.
- 41 D. Bůžek, J. Zelenka, P. Ulbrich, T. Ruml, I. Křížová, J. Lang, P. Kubát, J. Demel, K. Kirakci and K. Lang, *J. Mater. Chem. B*, 2017, **5**, 1815–1821.
- 42 A. S. Rury and R. J. Sension, *Chem. Phys.*, 2013, **422**, 220–228.
- 43 A. S. Rury, L. E. Goodrich, M. G. I. Galinato, N. Lehnert and R. J. Sension, *J. Phys. Chem. A*, 2012, **116**, 8321–8333.
- 44 E. S. Ryland, M.-F. Lin, M. A. Verkamp, K. Zhang, K. Benke, M. Carlson and J. Vura-Weis, *J. Am. Chem. Soc.*, 2018, **140**, 4691–4696.
- 45 H.-L. Jiang, D. Feng, K. Wang, Z.-Y. Gu, Z. Wei, Y.-P. Chen and H.-C. Zhou, *J. Am. Chem. Soc.*, 2013, **135**, 13934–13938.
- 46 A. De Vos, K. Hendrickx, P. Van Der Voort, V. Van Speybroeck and K. Lejaeghere, *Chem. Mater.*, 2017, **29**, 3006–3019.
- 47 Y. Horiuchi, T. Toyao, M. Saito, K. Mochizuki, M. Iwata, H. Higashimura, M. Anpo and M. Matsuoka, *J. Phys. Chem. C*, 2012, **116**, 20848–20853.
- 48 K. Hendrickx, D. E. P. Vanpoucke, K. Leus, K. Lejaeghere, A. Van Yperen-De Deyne, V. Van Speybroeck, P. Van Der Voort and K. Hemelsoet, *Inorg. Chem.*, 2015, **54**, 10701–10710.
- 49 K. Berg, S. Nordstrand, P. K. Selbo, D. T. T. Tran, E. Angell-Petersen and A. Høgstet, *Photochem. Photobiol. Sci.*, 2011, **10**, 1637–1651.
- 50 J. Fajer, D. Borg, A. Forman, R. Felton, D. Dolphin and L. Vegh, *Proc. Natl. Acad. Sci. U. S. A.*, 1974, **71**, 994–998.
- 51 R. Reed, R. Purrello, K. Prendergast and T. Spiro, *J. Phys. Chem.*, 1991, **95**, 9720–9727.
- 52 G. Dorough and F. Huennekens, *J. Am. Chem. Soc.*, 1952, **74**, 3974–3976.
- 53 N. D. Boscher, M. Wang and K. K. Gleason, *J. Mater. Chem. A*, 2016, **4**, 18144–18152.
- 54 P. Liao, X. Zhang, L. Zhang, X. Wang, W. Zhu, J. Sun, Y. Yan, L. Zhang, N. Chen and Z. Chen, *RSC Adv.*, 2016, **6**, 26186–26191.
- 55 C. D. Windle, M. W. George, R. N. Perutz, P. A. Summers, X. Z. Sun and A. C. Whitwood, *Chem. Sci.*, 2015, **6**, 6847–6864.
- 56 L. G. Arnaut, *Adv. Inorg. Chem.*, 2011, **63**, 187–233.

- 57 K. Kadish, K. M. Smith and R. Guilard, *The Porphyrin Handbook, Volume 10*, Elsevier, 2000.
- 58 F. A. Walker and U. Simonis, *Encycl. Inorg. Chem.*
- 59 J. Grodkowski, D. Behar, P. Neta and P. Hambright, *J. Phys. Chem. A*, 1997, **101**, 248–254.
- 60 T. Dhanasekaran, J. Grodkowski, P. Neta, P. Hambright and E. Fujita, *J. Phys. Chem. A*, 1999, **103**, 7742–7748.
- 61 D. Brault and M. Rougee, *Biochemistry*, 1974, **13**, 4598–4602.
- 62 R. Patra, S. Bhowmik, S. K. Ghosh and S. P. Rath, *Dalton Trans.*, 2010, **39**, 5795–5806.
- 63 F. Walker, M. Lo and M. Ree, *J. Am. Chem. Soc.*, 1976, **98**, 5552–5560.
- 64 R. Larsen, E. Findsen and R. Nalliah, *Inorganica Chim. Acta*, 1995, **234**, 101–107.
- 65 M. N. Podgorski, J. S. Harbort, T. Coleman, J. E. Stok, J. A. Yorke, L.-L. Wong, J. B. Bruning, P. Bernhardt, J. J. De Voss, J. R. Harmer and S. G. Bell, *Biochemistry*, 2020, **59**, 1038–1050.
- 66 S. Shankar, M. Peters, K. Steinborn, B. Krahwinkel, F. D. Soennichsen, D. Grote, W. Sander, T. Lohmiller, O. Ruediger and R. Herges, *Nat. Commun.*, 2018, **9**, 4750.
- 67 A. J. Morris, J. R. Stromberg and G. J. Meyer, *Inorg. Chem.*, 2010, **49**, 29–37.
- 68 C. Römel, J. Song, M. Tarrago, J. A. Rees, M. van Gastel, T. Weyhermüller, S. DeBeer, E. Bill, F. Neese and S. Ye, *Inorg. Chem.*, 2017, **56**, 4745–4750.
- 69 S. G. Cohen, A. Parola and G. H. Parsons, *Chem. Rev.*, 1973, **73**, 141–161.
- 70 S. Cohen and R. J. Baumgart, *J. Am. Chem. Soc.*, 1965, **87**, 2996–.
- 71 Y. Pellegrin and F. Odobel, *Comptes Rendus Chim.*, 2017, **20**, 283–295.
- 72 D. Chen, H. Xing, C. Wang and Z. Su, *J. Mater. Chem. A*, 2016, **4**, 2657–2662.
- 73 J.-S. Qin, S. Yuan, L. Zhang, B. Li, D.-Y. Du, N. Huang, W. Guan, H. F. Drake, J. Pang, Y.-Q. Lan, A. Alsalmé and H.-C. Zhou, *J. Am. Chem. Soc.*, 2019, **141**, 2054–2060.
- 74 H. Schwarz, *J. Phys. Chem.*, 1982, **86**, 3431–3435.
- 75 D. D. M. Wayner, D. J. McPhee and D. Griller, *J. Am. Chem. Soc.*, 1988, **110**, 132–137.
- 76 R. N. Sampaio, D. C. Grills, D. E. Polyansky, D. J. Szalda and E. Fujita, *J Am Chem Soc*, 2020, **16**.
- 77 T. Zhang, A. Solé-Daura, H. Fouilloux, J. M. Poblet, A. Proust, J. J. Carbó and G. Guillemot, *Chemcatchem*, 2021, **13**, 1220–1229.
- 78 W. M. Campbell, A. K. Burrell, D. L. Officer and K. W. Jolley, *Coord. Chem. Rev.*, 2004, **248**, 1363–1379.
- 79 D. Chen, D. Yang, J. Geng, J. Zhu and Z. Jiang, *Appl. Surf. Sci.*, 2008, **255**, 2879–2884.
- 80 K. Chaitanya, X.-H. Ju and B. M. Heron, *RSC Adv.*, 2014, **4**, 26621–26634.
- 81 J.-D. Chai and M. Head-Gordon, *Phys. Chem. Chem. Phys.*, 2008, **10**, 6615–6620.
- 82 M. J. Frisch, G. W. Trucks, H. B. Schlegel, G. E. Scuseria, M. A. Robb, J. R. Cheeseman, G. Scalmani, V. Barone, G. A. Petersson and H. Nakatsuji, Gaussian 16, Revision B.01, M. J. Frisch, G. W. Trucks, H. B. Schlegel, G. E. Scuseria, M. A. Robb, J. R. Cheeseman, G. Scalmani, V. Barone, G. A. Petersson, H. Nakatsuji, X. Li, M. Caricato, A. V. Marenich, J. Bloino, B. G. Janesko, R. Gomperts, B. Mennucci, H. P. Hratchian, J. V. Ortiz, A. F. Izmaylov, J. L. Sonnenberg, D. Williams-Young, F. Ding, F. Lipparini, F. Egidi, J. Goings, B. Peng, A. Petrone, T. Henderson, D. Ranasinghe, V. G. Zakrzewski, J. Gao, N. Rega, G. Zheng, W. Liang, M. Hada, M. Ehara, K. Toyota, R. Fukuda, J. Hasegawa, M. Ishida, T. Nakajima, Y. Honda, O. Kitao, H. Nakai, T. Vreven, K. Throssell, J. A. Montgomery, Jr., J. E. Peralta, F. Ogliaro, M. J. Bearpark, J. J. Heyd, E. N. Brothers, K. N. Kudin, V. N. Staroverov, T. A. Keith, R. Kobayashi, J. Normand, K. Raghavachari, A. P. Rendell, J. C. Burant, S. S. Iyengar, J. Tomasi, M. Cossi, J. M. Millam, M. Klene, C. Adamo, R. Cammi, J. W. Ochterski, R. L. Martin, K. Morokuma, O. Farkas, J. B. Foresman, and D. J. Fox, Gaussian, Inc., Wallingford CT, 2016.
- 83 M. M. Francl, W. J. Pietro, W. J. Hehre, J. S. Binkley, M. S. Gordon, D. J. DeFrees and J. A. Pople, *J. Chem. Phys.*, 1982, **77**, 3654–3665.
- 84 P. C. Hariharan and J. A. Pople, *Theor. Chim. Acta*, 1973, **28**, 213–222.
- 85 W. J. Hehre, R. Ditchfield and J. A. Pople, *J. Chem. Phys.*, 1972, **56**, 2257–2261.
- 86 P. J. Hay and W. R. Wadt, *J. Chem. Phys.*, 1985, **82**, 270–283.
- 87 A. W. Ehlers, M. Böhme, S. Dapprich, A. Gobbi, A. Höllwarth, V. Jonas, K. F. Köhler, R. Stegmann, A. Veldkamp and G. Frenking, *Chem. Phys. Lett.*, 1993, **208**, 111–114.
- 88 E. Cancès, B. Mennucci and J. Tomasi, *J. Chem. Phys.*, 1997, **107**, 3032–3041.
- 89 N. Planas, J. E. Mondloch, S. Tussupbayev, J. Borycz, L. Gagliardi, J. T. Hupp, O. K. Farha and C. J. Cramer, *J. Phys. Chem. Lett.*, 2014, **5**, 3716–3723.
- 90 R. Limvorapitux, H. Chen, M. L. Mendonca, M. Liu, R. Q. Snurr and S. T. Nguyen, *Catal. Sci. Technol.*, 2019, **9**, 327–335.
- 91 R. Bauernschmitt and R. Ahlrichs, *Chem. Phys. Lett.*, 1996, **256**, 454–464.
- 92 M. A. L. Marques and E. K. U. Gross, *Annu. Rev. Phys. Chem.*, 2004, **55**, 427–455.
- 93 J. Heyd, G. E. Scuseria and M. Ernzerhof, *J. Chem. Phys.*, 2003, **118**, 8207–8215.
- 94 A. Aziz, A. R. Ruiz-Salvador, N. C. Hernandez, S. Calero, S. Hamad and R. Grau-Crespo, *J. Mater. Chem. A*, 2017, **5**, 11894–11904.
- 95 D. Andrae, U. Häußermann, M. Dolg, H. Stoll and H. Preuß, *Theor. Chim. Acta*, 1990, **77**, 123–141.
- 96 M. Dolg, U. Wedig, H. Stoll and H. Preuss, *J. Chem. Phys.*, 1987, **86**, 866–872.